Available online at www.sciencedirect.com
ScienceDirect
Geochimica et Cosmochimica Acta 74 (2010) 3232–3245
Geochimica et Cosmochimica Acta
www.elsevier.com/locate/gca

Formation of nano-crystalline todorokite from biogenic Mn oxides

Xiong Han Feng [a,1], Mengqiang Zhu [a], Matthew Ginder-Vogel [a,b], Chaoying Ni [c], Sanjai J. Parikh [a,2], Donald L. Sparks [a,b,*]

[a] *Environmental Soil Chemistry Research Group, Department of Plant and Soil Sciences and Center for Critical Zone Research, 152 Townsend Hall, University of Delaware, Newark, DE 19716, USA*
[b] *Delaware Environmental Institute, University of Delaware, Newark, DE 19716, USA*
[c] *Department of Materials Science and Engineering, 201 Dupont Hall, University of Delaware, Newark, DE 19716, USA*

Received 15 May 2009; accepted in revised form 3 March 2010; available online 12 March 2010

Abstract

Todorokite, as one of three main Mn oxide phases present in oceanic Mn nodules and an active MnO_6 octahedral molecular sieve (OMS), has garnered much interest; however, its formation pathway in natural systems is not fully understood. Todorokite is widely considered to form from layer structured Mn oxides with hexagonal symmetry, such as vernadite (δ-MnO_2), which are generally of biogenic origin. However, this geochemical process has not been documented in the environment or demonstrated in the laboratory, except for precursor phases with triclinic symmetry. Here we report on the formation of a nanoscale, todorokite-like phase from biogenic Mn oxides produced by the freshwater bacterium *Pseudomonas putida* strain GB-1. At long- and short-range structural scales biogenic Mn oxides were transformed to a todorokite-like phase at atmospheric pressure through refluxing. Topotactic transformation was observed during the transformation. Furthermore, the todorokite-like phases formed via refluxing had thin layers along the c^* axis and a lack of c^* periodicity, making the basal plane undetectable with X-ray diffraction reflection. The proposed pathway of the todorokite-like phase formation is proposed as: hexagonal biogenic Mn oxide → 10-Å triclinic phyllomanganate → todorokite. These observations provide evidence supporting the possible bio-related origin of natural todorokites and provide important clues for understanding the transformation of biogenic Mn oxides to other Mn oxides in the environment. Additionally this method may be a viable biosynthesis route for porous, nano-crystalline OMS materials for use in practical applications.

1. INTRODUCTION

Mn oxides are environmentally ubiquitous and an important source of reactive mineral surfaces in the environments. There are over 30 known Mn oxide/hydroxide minerals resulting from the numerous environmental Mn oxidation states [Mn(II), Mn(III) and Mn(IV)] and an array of atomic arrangements (McKenzie, 1989; Dixon and Skinner, 1992; Post, 1999). These minerals participate in a variety of chemical and biological reactions that affect the water quality of marine and soil systems (Villalobos et al., 2003; Tebo et al., 2004; Webb et al., 2005a), and due to their reactivity have been called "scavengers of the sea" (Goldberg, 1954). The basic building block of Mn oxides is the

* Corresponding author at: Environmental Soil Chemistry Research Group, Department of Plant and Soil Sciences and Center for Critical Zone Research, 152 Townsend Hall, University of Delaware, Newark, DE 19716, USA. Tel.: +1 302 831 6378; fax: +1 302 831 0605.
E-mail address: dlsparks@udel.edu (D.L. Sparks).
[1] Present address: College of Resources and Environment, Huazhong Agricultural University, Wuhan 430070, PR China.
[2] Present address: Department of Land, Air and Water Resources, One Shields Avenue, The University of California, Davis, CA 95616, USA.

0016-7037/$ - see front matter © 2010 Elsevier Ltd. All rights reserved.
doi:10.1016/j.gca.2010.03.005

MnO_6 octahedron. These octahedra can be assembled through corner and/or edge sharing into a variety of structures that fall into two basic categories: (1) layer structures (phyllomanganates) and (2) chain, or tunnel structures (tectomanganate) (McKenzie, 1989; Dixon and Skinner, 1992; Post, 1999). According to the tunnel size, tectomanganates can be denoted as $T(m \times n)$. Todorokite, a family of tunnel structure Mn oxides with a $T(3 \times 3)$ array of edge-shared MnO_6 octahedra, is commonly associated with ferromanganese oxides from marine (Burns and Burns, 1978a; Chukhrov et al., 1979; Mellin and Lei, 1993; Takahashi et al., 2007) and terrestrial (Turner and Buseck, 1981; McKeown and Post, 2001; Manceau et al., 2007) settings. Mn oxide minerals are of potential economic interest because they are often enriched in Co, Ni, Cu and other strategic metals, including platinum group and rare earth elements (Post, 1999; Glasby, 2006). In addition, todorokite has many potential industrial applications, including use as sorbents, heterogeneous catalysts, sensors, and rechargeable battery cathodes (Shen et al., 1993; Vileno et al., 1998; Ching et al., 1999; Feng et al., 1999; Suib, 2008; Cui et al., 2009a).

Many of these Mn oxides are formed by microbial oxidation of soluble Mn(II). In fact Mn-oxidizing biota (i.e., bacteria and fungi) are commonly distributed throughout freshwater, ocean, and soil environments and catalyze the oxidation of Mn(II) at faster rates than abiotic processes (Nealson et al., 1988; Takematsu et al., 1988; Tebo et al., 2004). Recent studies characterizing microbial Mn(II) oxidation products reveal that they are exclusively X-ray amorphous, hexagonal, layer type Mn oxides with nanoparticle size similar to δ-MnO_2 (Bargar et al., 2005, 2009; Webb et al., 2005a,b; Miyata et al., 2006; Saratovsky et al., 2006; Villalobos et al., 2006). Reaction of Mn(II) and/or coexisting ions with the primary biogenic Mn oxide mineral yields abiotic secondary products, including 10-Å Na phyllomanganate, feitknechtite, hausmannite and manganite (Mandernack et al., 1995; Bargar et al., 2005). The occurrence of diverse Mn oxides in surface environments may result from secondary products of biogenic Mn oxidation (Tebo et al., 2004; Villalobos et al., 2003, 2006; Bargar et al., 2005, 2009).

The conversion pathways of biogenic Mn oxides into other Mn oxides, especially tunnel structure Mn oxides (e.g., todorokite), remains poorly understood. Although todorokite is often found associated with Mn oxides of microbial origin in ocean nodules, the pathways and mechanisms of todorokite formation from biogenic Mn oxides in nature are currently unknown (Burns and Burns, 1978b; Siegel and Turner, 1983; Mandernack et al., 1995; Post, 1999; Buatier et al., 2004; Bodei et al., 2007). This is largely due to difficulty simulating the geochemical processes involved in the mineralogical transformation from layered, biogenic Mn oxides into tunnel structure Mn oxides. These difficulties stem from the length of time these processes take at room temperature (Cui et al., 2006); additionally identification of poorly crystalline phases in a mixed system is problematic. Mn oxide minerals formed by the freshwater *Leptothrix discophora* SP6 were initially thought to have a todorokite-like tunnel structure (Kim et al., 2003); however, further investigation indicated the biogenic product actually possessed a layered topology (Saratovsky et al., 2006). In the presence of U(VI) the marine bacterium *Bacillus* sp. strain SG-1 forms poorly ordered Mn oxide tunnel structures, similar to todorokite (Webb et al., 2006); however, this phase has not been identified in environmental systems. Synthetic todorokites are generally obtained from modifying a layer structured Mn oxide with triclinic symmetry via a hydrothermal chemical route at relatively high temperature and pressure (Golden et al., 1986; Shen et al., 1993; Feng et al., 1995, 1998; Vileno et al., 1998; Ching et al., 1999; Luo et al., 1999; Liu et al., 2005). The formation of todorokite is greatly accelerated under mild reflux conditions at atmospheric pressure, enabling the simulation of formation processes for naturally occurring todorokite (Feng et al., 2004; Cui et al., 2006, 2008, 2009a,b). Here we describe the transformation of biogenic Mn oxide into a todorokite-like phase. The transformation products were characterized using X-ray absorption near edge structure (XANES) and extended X-ray absorption fine structure (EXAFS) spectroscopies, synchrotron-based X-ray diffraction (SR-XRD), transmission electron microscopy (TEM), field emission gun scanning electron microscopy (FEG-SEM) and high-resolution transmission electron microscopy (HR-TEM). We also propose a potential transformation pathway and mechanism for biogenic Mn oxides transformation into todorokite-like minerals.

2. EXPERIMENTAL METHODS

2.1. Biogenic Mn oxide production

Biogenic Mn oxides were produced by cultures of *Pseudomonas putida* strain GB-1, provided by B.M. Tebo (Oregon Health and Science University). Bacteria were grown in 500 mL *L. discophora* media in 1800 mL Erlenmeyer flasks at 30 °C and 200 rpm in a temperature-controlled incubator with an orbital shaker. The *Leptothrix* media contained 0.5 g L^{-1} yeast extract and casamino acids, 1 g L^{-1} glucose, 10 mM HEPES buffer (pH 7.5), 2 mM $CaCl_2$, 3.3 mM $MgSO_4$, 3.7 μM $FeCl_3$ and 1 mL trace element solution (10 mg/L $CuSO_4{\cdot}5H_2O$, 44 mg/L $ZnSO_4{\cdot}7H_2O$, 20 mg/L $CoCl_2{\cdot}6H_2O$, and 13 mg/L $Na_2MoO_4{\cdot}2H_2O$) (Boogerd and de Vrind, 1987). Inoculum cultures were prepared by growing bacteria from a *L. discophora* agar plate in MSTG media (2 mM $(NH_4)_2SO_4$, 0.25 mM $MgSO_4$, 0.4 mM $CaCl_2$, 0.15 mM KH_2PO_4, 0.25 mM Na_2HPO_4, 10 mM HEPES, 0.01 mM $FeCl_3$, 0.01 mM EDTA, 1 mM glucose, and 1 mL trace metal solution) for 12 h at 30 °C (Parikh and Chorover, 2005). Cells were harvested after 19 h, via centrifugation at 10,000 RCF, at which time the cells have a maximum oxidizing capacity. The harvested cells were rinsed with a solution of 10 mM HEPES at pH 7 to remove metabolites from the spent media. The cells harvested from each 500-mL culture were re-suspended in 1 L of autoclaved 50 mM NaCl and 10 mM HEPES at pH 7. Filter-sterilized $MnSO_4$ solution was added to the above solution after autoclaving to a final concentration of 100 μM. The suspensions were shaken at 200 rpm at 30 °C for 48 h, at which time the Mn(II) in the solution, measured by the formaldoxime colorimetric method (Burle and Kirby-Smith, 1979), was exhausted. The

biogenic Mn oxides were then collected by centrifugation at 3000 RCF. At this centrifugal speed, non-membrane bound EPS (exopolymer substances) remained in the supernatant and was then discarded. The biogenic Mn oxides were then re-suspended in 50 mM NaCl and 10 mM HEPES (pH 7) and allowed to settle overnight. The EPS in this supernatant was then removed to further purify the biogenic Mn oxides. This procedure was repeated several times to ensure that only trace amounts of EPS remained associated with the biogenic Mn oxides.

2.2. Transformation of the biogenic Mn oxide

After purification as described above, the biogenic Mn oxide, collected from three 1-L 100 μM Mn(II), 50 mM NaCl and 10 mM HEPES solutions, was mixed before re-suspension in 250 mL 1 M $MgCl_2$ solution and exchanged for 12 h. After centrifugation at 10,000 RCF, the Mg^{2+}-exchanged biogenic Mn oxide (hereafter BMO-Mg) was re-suspended in a 250 mL 1 M $MgCl_2$ solution at pH 5.1 in a 500 mL Erlenmyer flask connected with a glass condenser cooled by using tap water in the outer jacket. Then the suspension was heated to and kept at reflux under stirring on a combined hot-plate and magnetic-stirrer. Aliquot suspensions (50-mL) were taken and cooled down to room temperature at 8 h, 24 h time intervals. After 48 h of reflux, the heat was stopped and the residual suspension was cooled to room temperature. The refluxed solid products, BMO-8 h, BMO-24 h and BMO-48 h designated for products refluxed for 8, 24 and 48 h, respectively, were obtained via filtering with 0.22 μm filters and then washed with 25 mL of distilled deionized water for two times. The pH and Mn(II) in the supernatants were determined using a pH meter and Inductively Coupled Plasma Atomic Emission Spectrometry (ICP-AES), respectively.

2.3. Preparation of the reference Mn oxide minerals

Todorokite (hereafter Todorokite-STD) was prepared using a previously described reflux method (Feng et al., 2004). Cryptomelane was synthesized by modifying the procedure of McKenzie (McKenzie, 1971; Feng et al., 2007). δ-MnO_2, a disordered hexagonal layer manganate (Villalobos et al., 2003, 2006), was prepared using a "redox" method with stoichiometric amounts of $KMnO_4$ and $MnCl_2$ (Gadde and Laitinen, 1974). Acid birnessite (hexagonal birnessite), was prepared by reducing $KMnO_4$ with concentrated HCl at boiling temperature (McKenzie, 1971). Random stacked birnessite (RSB), a disordered triclinic birnessite, was synthesized through oxidation of $Mn(OH)_2$ by O_2 in alkali medium (Yang and Wang, 2002). Triclinic birnessite was prepared by aging the RSB suspension at 313–373 K (Yang and Wang, 2002). MnO, Mn_2O_3 (bixbyite) and MnO_2 (pyrolusite) were purchased from Aldrich. The purity of these phases was confirmed by X-ray diffraction.

2.4. X-ray absorption fine structure (XAFS) spectroscopy

Prior to XAFS spectroscopic analyses, biogenic Mn oxide, Mg^{2+} exchanged minerals and the refluxing products were washed, centrifuged, and re-suspended several times to remove the loosely bound Mn^{2+} and Mg^{2+} remaining from the corresponding treatments. After vacuum filtration, the XAFS samples were prepared by mounting the wet paste in thin (~1 mm) plastic holders in a 20 × 5 mm slot which was sealed with Mylar film. Mn K-edge XAFS data were collected using beamline X-11A at the National Synchrotron Light Source (NSLS), Brookhaven National Laboratory (Upton, NY). The electron beam energy was 2.5–2.8 GeV, with a maximum beam current of 300 mA. The monochromator consisted of two parallel, channel-cut Si(1 1 1) crystals with a vertical entrance slit opening of ~0.5 mm. The beam size on the sample was maintained at 2 × 10 mm. The samples were mounted 45° to the incident beam and Mn K-edge EXAFS data were collected over the energy range 6339–7286 eV in fluorescence mode using an Ar filled Lytle detector. An internal reference (Mn^0) was collected concurrently ($E_0 = 6539$ eV) for energy calibration. The first ionization chamber was filled with 50% N_2 and 50% He, while the second and third ionization chambers were filled with 100% N_2. A 3 μx Cr filter, one to two sheets of Al foil, and Soller slits were used to limit the impact of elastic and Compton radiation as well as filter the fluorescence signal. The fluorescence and transmission data of each sample were compared to check for self-absorption effects, which were not observed. Harmonics were eliminated from the incident beam by detuning the monochromator by 30% of I_0. Multiple scans ($\geqslant 3$) were collected for each sample to improve statistics. Reference Mn oxide mineral samples were prepared for analysis by mixing finely ground powder of each mineral with boron nitride (BN) to ~10% Mn by weight. Each sample was then loaded into an individual acrylic sample holder and sealed with Kapton tape. Non-adhesive Kapton film was used to seal the sample cell to avoid any interaction of the sample with the tape adhesive. The Mn K-edge XAFS data were collected from reference Mn oxide minerals in transmission mode. Reproducibility of the transmission spectra collected at several different locations and at a long duration on selected samples confirmed sample homogeneity and no sample damage by the X-ray radiation. All XAFS data reduction and analysis was performed using SIXPack (Webb, 2005). Mn K-edge EXAFS data were fit in R space using a full multiple scattering model based on a phyllomanganate structure (Webb et al., 2005a).

2.5. Synchrotron-based X-ray diffraction (SR-XRD)

SR-XRD patterns were recorded from wet paste samples in transmission geometry with a MAR345 image plate at an incident X-ray energy of 12,732 eV (0.9742 Å) at SSRL beamline 11-3. Wet sample slurries were placed in an aluminium sample cell between Lexan (polycarbonate) windows. Two-dimensional XRD patterns were calibrated with lanthanum hexaboride (LaB_6) and integrated to one-dimensional patterns with Fit2d (Hammersley et al., 1996). The background contributions due to the Lexan windows and water in the sample were removed using XRDbs (http://ssrl.slac.stanford.edu/~swebb/xrdbs.htm).

2.6. FEG-SEM and TEM analysis

FEG-SEM and TEM micrographs were collected at the Bio-imaging Center at Delaware Biotechnology Institute at the University of Delaware. Morphology of the biogenic Mn oxide and the refluxed products were imaged with a Hitachi S-4700 field emission gun scanning electron microscope and a Zeiss CEM 902 TEM. Prior to analysis the samples were fixed using glutaraldehyde, postfixed with 1% osmium tetraoxide, and then dehydrated with a series of ethanol–water solutions. After critical point drying, the samples were mounted on double-sided carbon tape and carbon coated for FEG-SEM observation. For TEM analysis the samples were fixed with glutaraldehyde, postfixed with 1% osmium tetraoxide, stained with 0.5% uranyl acetate, and then dehydrated with acetone. Then they were embedded in resin and thin sectioned with a glass knife on a microtome for TEM observation.

2.7. HR-TEM analysis

The HR-TEM analyses were performed on the above TEM samples and sample suspensions air dried on a holey carbon grid with a JEOL JEM 2010 FEF electron microscope operated at 200 kV.

3. RESULTS

3.1. XANES and EXAFS spectroscopy

3.1.1. XANES

The lineshapes of Mn K-edge XANES spectra are sensitive to changes in oxidation state (peak position) and local coordination environment (peak shape) (Villalobos et al., 2003). XANES was used as the principal method to determine the average oxidation state (AOS) and coordination geometry of Mn in samples maintained under natural conditions (Villalobos et al., 2003, 2006; Webb et al., 2005a). A standard curve was generated using the edge positions of MnO_x standards with known oxidation states (Fig. 1). The AOS of Mn in BMO and BMO-Mg was found to be 3.8 ± 0.3, the AOS of BMO-8 h, BMO-24 h, BMO-48 h was 3.6 ± 0.3 and the AOS of Todorokite-STD was 3.7 ± 0.3. A double-hump in the range from 6540 to 6545 eV, arising from bound state quadrupole-allowed 1s to 3d transitions (Saratovsky et al., 2006), was found in the pre-edge region of the X-ray absorption spectrum of the biogenic Mn oxide, each refluxed product and todorokite (Figs. 1 and 2), suggesting that these Mn cations are octahedrally coordinated. Therefore, the refluxed products of BMO-Mg consist primarily of Mn(IV), with a fraction of Mn at lower valences, and exhibit octahedral coordination geometry, common to phyllomanganates and tectomanganates.

3.1.2. EXAFS

EXAFS spectroscopy probes the average local coordination environment around Mn to approximately 6 Å (Villalobos et al., 2003, 2006; Webb et al., 2005a,b, 2006; Saratovsky et al., 2006, 2009) and was used to quantitatively compare BMO, BMO-Mg and the refluxed products with todorokite. The *k* space and *R* space EXAFS spectrum for BMO, as shown in Fig. 3, are consistent with those published for the biogenic Mn oxides produced by other model Mn oxidizing bacteria, such as *P. putida* strain MnB1 (Villalobos et al., 2003, 2006), *L. discophora* SP6 (Kim et al., 2003; Saratovsky et al., 2006) and *Bacillus* sp. strain SG-1 (Webb et al., 2005a,b, 2006).

The region of the EXAFS spectrum from 7.5 to 9.5 $Å^{-1}$ varies the most between tunnel and layer manganate structures (McKeown and Post, 2001; Manceau et al., 2005; Webb et al., 2006). After the reflux treatment, this region shows the most dramatic changes (Fig. 3a). Instead of distinct peaks, two steadily rising slopes gradually appear between 7.5 and 9.5 $Å^{-1}$, indicative of the formation of a

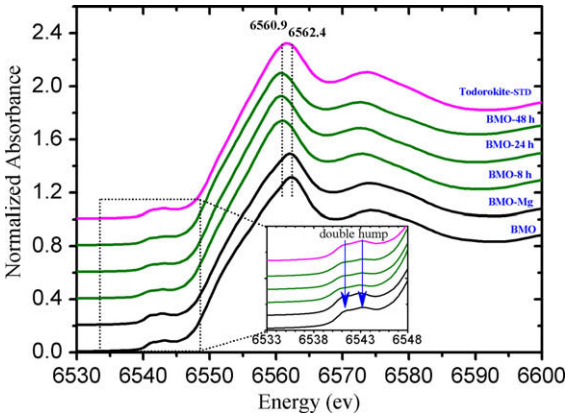

Fig. 1. XANES spectra of BMO, BMO-Mg, BMO-8 h, BMO-24 h, BMO-48 h and Todorokite-STD. The white lines for BMO and BMO-Mg are at around 6562.4 eV, and those for BMO-8 h, BMO-24 h and BMO-48 h are 6560.9 eV. The white line for the todorokite standard is 6561.5 eV.

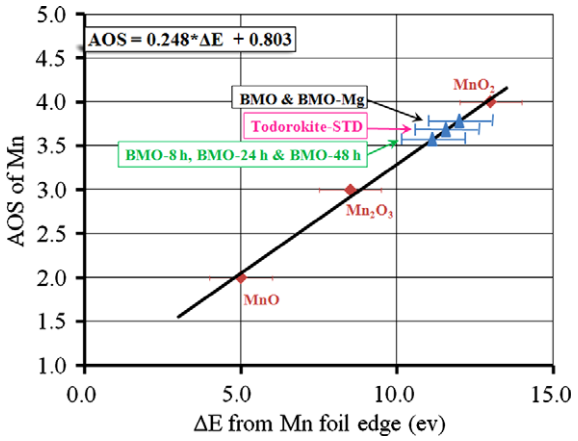

Fig. 2. Quantification of AOS in BMO, BMO-Mg, BMO-8 h, BMO-24 h, BMO-48 h and Todorokite-STD. AOS was determined by location of absorption edge energies (inflection point) in reference compounds of known oxidation states. The edge energies observed in the XANES of MnO, Mn_2O_3 (bixbyite) and MnO_2 (pyrolusite) were used to calibrate AOS as a function of edge energy.

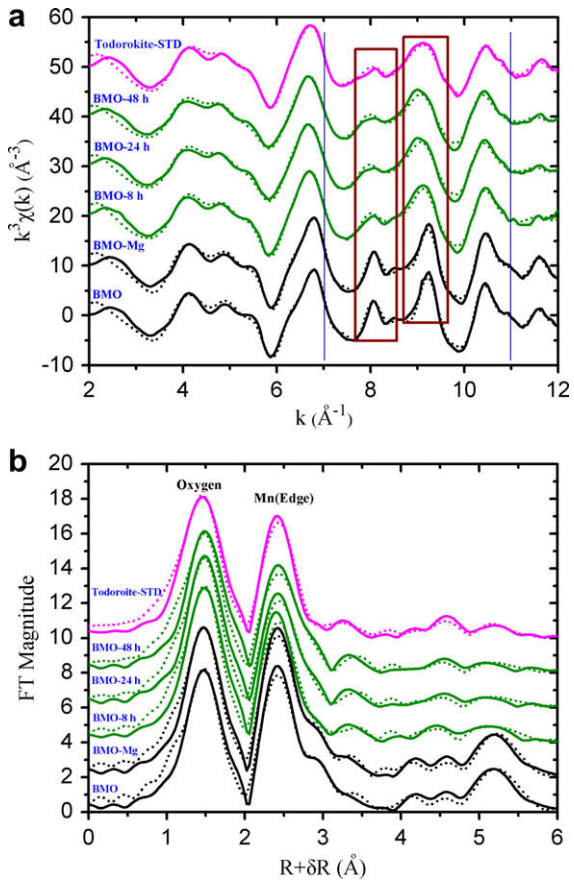

Fig. 3. Mn K-edge k^3-weighted EXAFS (a) and Fourier transformed EXAFS (b) spectra (solid line) with best fit overlaid (dotted line) from the full multiple scattering manganese EXAFS model (Webb et al., 2005a) for *Pseudomonas putida* GB-1 bacterial cell oxidation system and the intermediate products after Mg^{2+} exchange and reflux treatment for the different times as well as the synthesized todorokite standard. Note the change in diagnostic features in the k space region between $k \sim 7$–11 Å^{-1} which is highlighted by the vertical lines.

tunnel structure manganate during refluxing (Webb et al., 2005a, 2006; Bodei et al., 2007). In contrast to BMO-Mg, the Fourier transform of the EXAFS spectra of the refluxed products gradually reveals typical characteristics of transformation of phyllomanganate to tectomanganate (Webb et al., 2005a). These characteristics include a decrease in the relative amplitude of peaks for the first shell edge-sharing Mn and the Mn–Mn multiple scattering over the refluxing time from 8 to 48 h (Fig. 3b). Quantitative fitting parameters (Table 1), using the full multiple scattering Mn EXAFS model (Webb et al., 2005a), confirmed a decrease in Mn site occupancy (focc), an increase in dihedral angle from out-of-plane bending (β), and an increase in the number of corner sharing Mn octahedra due to formation of a tunnel structure Mn oxide (Webb et al., 2005a, 2006). Mn EXAFS spectra of the refluxed products are most similar to $T(3 \times 3)$ tunnel structure manganate (i.e., todorokite) rather than cryptomelane ($T(2 \times 2)$), pyrolusite ($T(1 \times 1)$) (Fig. 4a and b) or psilomelane ($T(2 \times 3)$) (McKeown and Post, 2001; Kim et al., 2003). Furthermore, the fitting parameters, including focc, β, and the number of corner sharing Mn, which are sensitive to the size of the tunnel (Webb et al., 2005a), for the refluxed products, BMO-24 h and BMO-48 h, are similar to those of Todorokite-STD (Table 1).

3.2. SR-XRD

SR-XRD analysis was used to investigate the evolution of the long-range structure of the biogenic MnO_x during the refluxing process. Diffraction patterns of BMO and BMO-Mg are similar, and exhibit two broad peaks at 0.246 and 0.142 nm resulting from the reflection of the *ab*-layer plane (Villalobos et al., 2003, 2006; Saratovsky et al., 2006) of the biogenic Mn oxides (Fig. 5). The absence of a basal reflection peak for BMO and BMO-Mg (0.7 or 1.0 nm) demonstrates the poorly ordered stacking of adjacent layers, or discrete layers as in the case of δ-MnO_2 (Villalobos et al., 2006; Bodei et al., 2007). Diffraction patterns of the refluxed products have broad peaks centered at 0.477, 0.248, 0.154, 0.146 and 0.142 nm, all of which can be attributed to the monoclinic todorokite structure (JCPDS 38-475). The peak at ~0.24 nm has a similar composite shape to that for todorokite and is diagnostic for todorokite, differentiating todorokite from other phyllomanganates with a similar basal plane reflections (~1.0 nm), such as 1 nm vernadite (Bodei et al., 2007).

3.3. Electron microscopy

FEG-SEM images (Fig. 6a) of the biogenic oxide show stringy, rope-like features, indicative of membrane bound EPS desiccation during FEG-SEM sample preparation (Toner et al., 2005). The morphology of the poorly crystalline biogenic oxide particles consists of fibrillar thin planes with dimensions of ~10 nm wide by ~100 nm long surrounding the oblate spheroid shape of bacterial cells (Fig. 6b and c), similar to that reported for Mn oxides produced by *L. discophora* SP6 (Saratovsky et al., 2006) and *P. putida* strain MnB1 (Villalobos et al., 2003). After refluxing, the Mn oxide particles maintained similar fibrillar morphology with slightly smaller dimensions resulting from partial reductive dissolution by residual biological substances. This indicates a topotactic transformation process, in which the product preserves the features of the precursor in morphology and crystallization, as is the case for todorokite formation from phyllomanganate precursors (Bodei et al., 2007). The Mn oxide particles also became more closely associated with the bacterial cells, which became slightly distorted during refluxing (Fig. 6d and e). In comparison, the surface of BMO-48 h became smooth, lacking the original biofilm, which may have become mixed with the Mn oxide particles during refluxing. An HR-TEM image of an individual Mn oxide fiber of BMO-48 h shows the lattice fringes with a common dimension of ~1 nm along the a^* direction (Fig. 6f), indicative of a tunnel width of three MnO_6 octahedra as found in todorokite (Turner and Buseck, 1981; Post and Bish, 1988; Post, 1999). Furthermore, ~0.5 nm lattice fringes in the a^* direction were also observed,

Table 1
Summary of EXAFS fitting parameters from the Mn K-edge using the full multiple scattering Mn oxide model (Webb et al., 2005a) for the biogenic oxide, the products after different treatments and the todorokite standard.

Sample	R[a]	χ^{2}[b]	focc	β (a-axis)	β (b-axis)	Shell[c]	CN[d]	Diat (Å)	σ^2
BMO	0.0226	2393.1	0.73(3)	0(3)	5(5)	Mn–O	4	1.85(2)	0.006(4)
						Mn–O	2	1.93(1)	0.002(4)
						Mn–Mn edge	2	2.81(1)	0.005(2)
						Mn–Mn edge	4	2.87(3)	
						Mn–O	4	3.47(6)	0.001(7)
						Mn–O	2	3.65(1)	
						Mn–Mn corner	0.9(3)	3.51(2)	0.010(3)
						Mn–Na interlyr	1.0(5)	4.11(3)	0.004(3)
						Mn–O	4	4.67(2)	0.002(1)
						Mn–O	8	4.81(8)	
						Mn–Mn diag	4	5.00(1)	0.005(1)
						Mn–Mn diag	2	5.20(2)	
						Mn–Mn next	2	5.53(3)	0.006(2)
						Mn–Mn next	4	5.85(2)	
BMO-Mg	0.019	2889.8	0.76(3)	0(3)	8(3)	Mn–O	4	1.85(1)	0.004(1)
						Mn–O	2	1.95(1)	0.001(1)
						Mn–Mn edge	2	2.81(1)	0.006(1)
						Mn–Mn edge	4	2.88(4)	
						Mn–O	4	3.46(1)	0.001(1)
						Mn–O	2	3.69(2)	
						Mn–Mn corner	0.5(5)	3.62(4)	0.009(1)
						Mn–Mg interlyr	0.5(5)	4.11(3)	0.001(6)
						Mn–O	4	4.68(3)	0.002(2)
						Mn–O	8	4.82(2)	
						Mn–Mn diag	4	5.01(1)	0.004(2)
						Mn–Mn diag	2	5.20(4)	
						Mn–Mn next	2	5.54(3)	0.006(2)
						Mn–Mn next	4	5.83(2)	
BMO-8 h	0.028	5077.6	0.68(3)	5(2)	16(4)	Mn–O	4	1.86(1)	0.004(1)
						Mn–O	2	1.95(1)	0.001(1)
						Mn–Mn edge	2	2.85(2)	0.007(1)
						Mn–Mn edge	4	2.88(1)	
						Mn–O	4	3.49(0.12)	0.001(1)
						Mn–O	2	3.64(4)	
						Mn–Mn corner	1.4(8)	3.42(2)	0.009(4)
						Mn–Mg interlyr	0.3(3)	4.01(5)	0.001(3)
						Mn–O	4	4.62(3)	0.011(2)
						Mn–O	8	4.73(2)	
						Mn–Mn diag	4	4.92(3)	0.006(2)
						Mn–Mn diag	2	5.06(6)	
						Mn–Mn next	2	5.53(8)	0.009(4)
						Mn–Mn next	4	5.62(4)	
BMO-24 h	0.033	16916.1	0.57(3)	6(3)	22(6)	Mn–O	4	1.86(1)	0.004(1)
						Mn–O	2	1.95(1)	0.001(1)
						Mn–Mn edge	2	2.86(2)	0.006(1)
						Mn–Mn edge	4	2.87(1)	
						Mn–O	4	3.46(1)	0.001(1)
						Mn–O	2	3.59(2)	
						Mn–Mn corner	2.1(1.1)	3.37(2)	0.012(5)
						Mn–Mg interlyr	0.5(0.3)	4.00(3)	0.001(2)
						Mn–O	4	4.61(8)	0.011(6)
						Mn–O	8	4.74(4)	
						Mn–Mn diag	4	4.93(4)	0.007(5)
						Mn–Mn diag	2	5.07(0.10)	
						Mn–Mn next	2	5.73(0.13)	0.007(6)
						Mn–Mn next	4	5.59(5)	
BMO-48 h	0.038	17923.2	0.53(3)	5(4)	22(4)	Mn–O	4	1.86(1)	0.004(1)
						Mn–O	2	1.96(1)	0.001(1)
						Mn–Mn edge	2	2.87(2)	0.006(1)

(*continued on next page*)

Table 1 (*continued*)

Sample	R[a]	χ^2[b]	focc	β (a-axis)	β (b-axis)	Shell[c]	CN[d]	Diat (Å)	σ^2
						Mn–Mn edge	4	2.87(1)	
						Mn–O	4	3.46(1)	0.001(1)
						Mn–O	2	3.59(3)	
						Mn–Mn corner	2.5(1.3)	3.36(2)	0.012(5)
						Mn–Mg interlyr	0.6(0.3)	4.01(3)	0.001(3)
						Mn–O	4	4.61(8)	0.011(6)
						Mn–O	8	4.74(4)	
						Mn–Mn diag	4	4.95(4)	0.007(5)
						Mn–Mn diag	2	5.08(0.10)	
						Mn–Mn next	2	5.73(0.13)	0.007(7)
						Mn–Mn next	4	5.59(5)	
Todorokite-STD	0.017	6614.8	0.55(2)	6(3)	19(3)	Mn–O	4	1.85(1)	0.004(1)
						Mn–O	2	1.96(1)	0.001(1)
						Mn–Mn edge	2	2.88(2)	0.007(1)
						Mn–Mn edge	4	2.86(1)	
						Mn–O	4	3.45(1)	0.001(1)
						Mn–O	2	3.56(2)	
						Mn–Mn corner	1.9(0.4)	3.38(1)	0.009(2)
						Mn–Mg interlyr	0.5(0.2)	3.96(2)	0.001(2)
						Mn–O	4	4.60(6)	0.009(4)
						Mn–O	8	4.77(3)	
						Mn–Mn diag	4	4.98(2)	0.009(2)
						Mn–Mn diag	2	5.00(5)	
						Mn–Mn next	2	5.70(5)	0.007(3)
						Mn–Mn next	4	5.57(2)	

[a] R factor.
[b] Chi squared.
[c] Mn–Mn edge, Mn–Mn corner, Mn–Mn diag, Mn–Mn next corner sharing Mn shell denote edge-sharing Mn shell, corner sharing Mn shell, diagonal Mn shell and next to diagonal Mn shell, respectively. Mn–Mg(Na) interlayer denotes interlayer Mg(Na) shell (Webb et al., 2005a).
[d] Fixed except for CN of Mn–Mn corner, Mn–Na interlayer and Mn–Mg interlayer.

probably due to the intergrowth of a narrow tunnel with one MnO_6 octahedron width, which is very common in the structure of natural and synthetic todorokite (Chukhrov et al., 1979; Turner et al., 1982; Golden et al., 1986; Feng et al., 2004; Bodei et al., 2007), or due to the orderly stacking of tunnel cations, Mg^{2+} or Mn^{2+}, in the center of a tunnel with a width of three MnO_6 octahedra.

4. DISCUSSION

4.1. Structural transformation of the biogenic Mn oxide after reflux treatment

Due to the low degree of crystallinity, nanometer dimensions and similar edge-sharing MnO_6 octahedral units that are arrayed in layers, as most layer and tunnel Mn oxides, structural characterization and identification of biogenic Mn oxides is often ambiguous when based solely on XRD analyses. For example, XRD patterns of biogenic Mn oxide, vernadite, buserite and todorokite are often indistinguishable and are prone to be confused in their identification due to their similar diffraction features (Burns et al., 1983, 1985; Giovanoli, 1985; Bodei et al., 2007; Saratovsky et al., 2009). Thus it can be explained why 10-Å vernadite, buserite and todorokite were initially regarded as the same Mn oxide phase named as 10-Å manganite according to the d space of basal plane diffraction (Buser and Grütter, 1956). Although todorokite formation by microbial mediation was reported by Takematsu et al. (1984, 1988), the identification of the product via XRD should be viewed with skepticism. The product is likely 10-Å phyllomanganate or buserite because it was transformed into birnessite with time. XAFS (XANES and EXAFS) spectroscopy, sensitive to local structure features, is a promising technique for the identification of biogenic origin Mn oxides. However, even with the aid of XAFS spectroscopy the identification can be ambiguous and erroneous such as in Kim et al. (2003). With careful comparison both in k and R space spectroscopy and fitting of EXAFS spectra the identification can be conclusive (Bargar et al., 2005, 2009; Webb et al., 2005a,b; Saratovsky et al., 2006, 2009; Villalobos et al., 2006).

In this paper, the comparison of spectra both in k and in R space among the original biogenic Mn oxide, the refluxed products and tunnel structure Mn oxides with different tunnel sizes was conducted. The original biogenic Mn oxide (BMO) possesses common structural features of primary biological oxidation products of Mn oxidizing bacteria and is similar to δ-MnO_2 or hexagonal birnessite based on its EXAFS spectral features, i.e., sharp peaks approximately at 8 and 9.2 $Å^{-1}$ in k space in the EXAFS spectrum (Fig. 3a), the high amplitude of peaks for the first shell edge-sharing Mn (2.87 Å) and the Mn–Mn multiple scattering at about 5.6 Å in the Fourier transform of the EXAFS

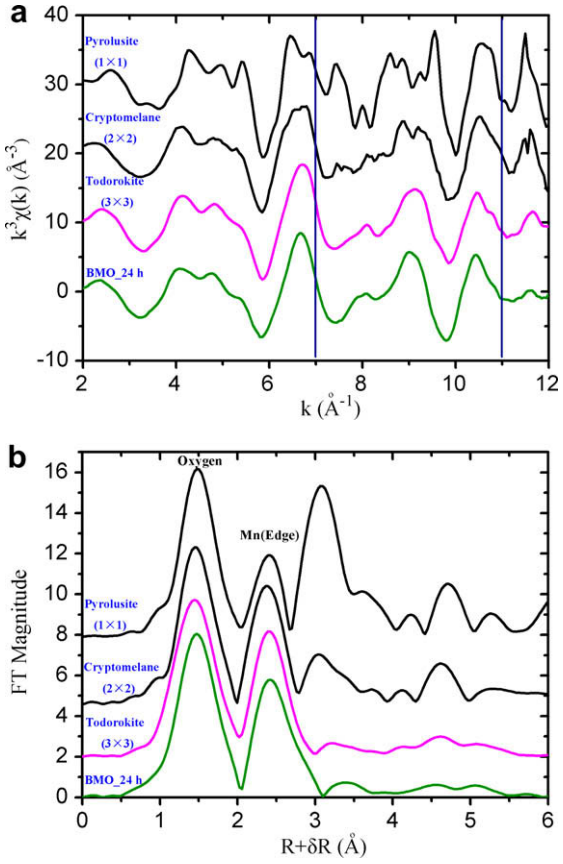

Fig. 4. Comparison of Mn K-edge k^3-weighted EXAFS (a) and Fourier transformed EXAFS (b) between BMO-24 h and different tunnel structured Mn oxide minerals [todorokite ($T(3 \times 3)$), cryptomelane ($T(2 \times 2)$) and pyrolusite ($T(1 \times 1)$)].

spectra (Fig. 3b). The $d(200, 110)/d(020, 310)$ ratio is $\sim\sqrt{3}$ (Fig. 5), which also exemplifies the hexagonal symmetry of BMO (Drits et al., 1997; Villalobos et al., 2003, 2006). The close similarity between BMO and BMO-Mg EXAFS spectra suggests that Mg^{2+} exchange does not change the local structure.

It is typically easy to tell todorokite from other tunnel Mn oxides, but more difficult to distinguish between disordered todorokite and disordered phyllomanganates. The comparison was also performed between the refluxed products and different phyllomanganates, such as δ-MnO_2, hexagonal birnessite, random stacked birnessite (RSB) and triclinic birnessite (Fig. 7). From the comparison both in k and in R space the product is different from any of the phyllomanganites. It can be seen that the spectra of the refluxed products and the EXAFS fitting results (Fig. 3 and Table 1), especially the results of vacancy site number (focc), corner sharing Mn number and out-of-plane bending angle (β) match very well with those of todorokite. Therefore, after the reflux treatment, Mg exchanged biogenic Mn oxide gradually transformed into a tunnel structure manganate similar to todorokite.

SR-XRD analyses further confirmed the transformation at long-range structural scale. There is an absence of the basal plane reflection (~1.0 nm) in the refluxed products XRD

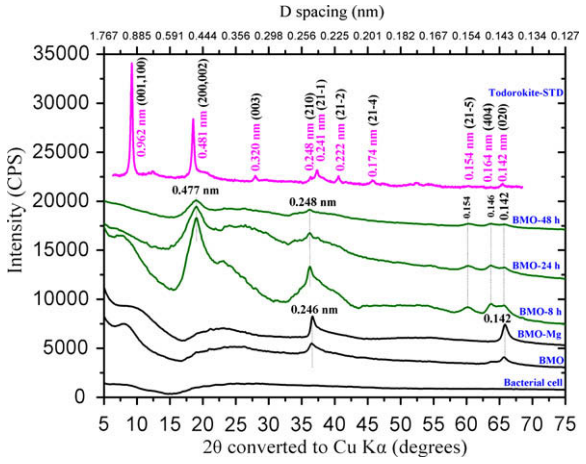

Fig. 5. Synchrotron X-ray diffraction patterns for the *Pseudomonas putida* GB-1 bacterial cell oxidation system and the intermediate products after Mg^{2+} exchange and reflux treatment for the different times compared to the XRD pattern of the synthesized todorokite standard.

patterns (Fig. 5), which is attributed to thin or disordered layer stacking along the c^* axis and the lack of c^* periodicity (Villalobos et al., 2006; Bodei et al., 2007; Bargar et al., 2009), as in case of the precursor BMO and BMO-Mg.

4.2. Comparison of the transformation of chemically synthesized birnessite to todorokite and natural todorokite formation

Natural todorokites typically occur as poorly crystallized nano-particles mixed with many other minerals. Synthesis of todorokite is a promising alternative to obtain todorokite samples for fundamental research and industrial application studies. Todorokite was first synthesized through autoclave treatment of 10-Å Mg^{2+} exchanged birnessite (Mg-buserite) at 155 °C (Golden et al., 1986, 1987). Another thermally stable version of todorokite can be synthesized by a similar hydrothermal treatment via oxidation of $Mn(OH)_2$ with $Mg(MnO_4)_2$ to prepare precursor birnessite in alkali media (Shen et al., 1993). Other hydrothermal methods for todorokite syntheses that use different birnessite preparation procedures or microwave heating have also been reported (Feng et al., 1995, 1998; Vileno et al., 1998; Ching et al., 1999; Luo et al., 1999; Liu et al., 2005). In addition to hydrothermal methods, a mild reflux procedure under atmospheric pressure was proposed to synthesize todorokite in our previous work (Feng et al., 2004). Therefore, preparation of Na-birnessite, exchange of 7-Å Na-birnessite with a cation (generally Mg^{2+} is used) to obtain a 10-Å buserite, and then hydrothermal or reflux treatment of 10-Å buserite at a relatively high temperature are common steps in todorokite syntheses.

The reflux treatments used to transform biogenic Mn oxide into todorokite are generally similar to those used to transform chemically synthesized birnessite into todorokite. However, the precursors are different, not only is our precursor biological in origin, without a basal plane dif-

fraction peak, but it also possesses hexagonal symmetry, distinct to other precursors which possess triclinic symmetry. Interestingly, in all reported todorokite synthesis procedures, the precursor minerals are exclusively triclinic birnessite, which forms in alkali media and has one third of $Mn(III)O_6$ octahedra in MnO_6 octahedral unit (Drits et al., 1997; Lanson et al., 2002).

Microbially mediated Mn(II) oxidation is believed to be the dominant source of Mn oxides in marine, freshwater and subsurface aquatic environments (Tebo et al., 2004; Webb et al., 2006; Bargar et al., 2009). The primary products of microbial Mn(II) oxidation are poorly crystallized layer Mn oxides with a hexagonal symmetry, similar to δ-MnO_2 (Tebo et al., 2004; Bargar et al., 2005, 2009; Webb et al., 2005a,b; Miyata et al., 2006; Saratovsky et al., 2006; Villalobos et al., 2006). Therefore, natural todorokites in the environment are considered to form from layer structured Mn oxides with hexagonal symmetry, such as vernadite (δ-MnO_2), which are generally of biogenic origin (Tebo et al., 2004; Webb et al., 2006; Bodei et al., 2007; Bargar et al., 2009). However, this transformation process has not been documented in the laboratory. Acid birnessite, synthesized in acidic media with a hexagonal symmetry, does not transform into todorokite through the same treatment, instead it converts to cryptomelane, ramsdellite and another unidentifiable phase (Fig. EA-1). Attempts to synthesize todorokite from 10-Å vernadite, with hexagonal symmetry, were also unsuccessful (Bodei et al., 2007).

Topotactic transformation from layer Mn oxides to todorokite was observed in both synthesized and natural todorokites (Chukhrov et al., 1979; Golden et al., 1986, 1987; Shen et al., 1993; Feng et al., 2004; Bodei et al., 2007). In these cases, todorokites formed *in situ* from precursor phyllomanganates, exhibited a morphology of platy matrix consisting of twinned fibers matted at 120° from one another, from which fiber crystals extended. The HR-TEM results indicate the topotactic transformation from biogenic Mn oxide to todorokite-like phase after refluxing. While we do not observe the twinned fibers in the refluxed products, this possibly results from the weakly crystallized BMO precursor with a low degree of 3D periodicity (Bodei et al., 2007). Due to the topotactic transformation from biogenic Mn oxide, the refluxed products have thin layers along the c^* axis and lack c^* periodicity. In addition because the 1 nm basal plane reflection is a doublet of the (1 0 0) and (0 0 1), the lack of 1 nm reflection indicated that the refluxed products also lack a^* periodicity. Intergrowth of $T(3 \times n)$ building

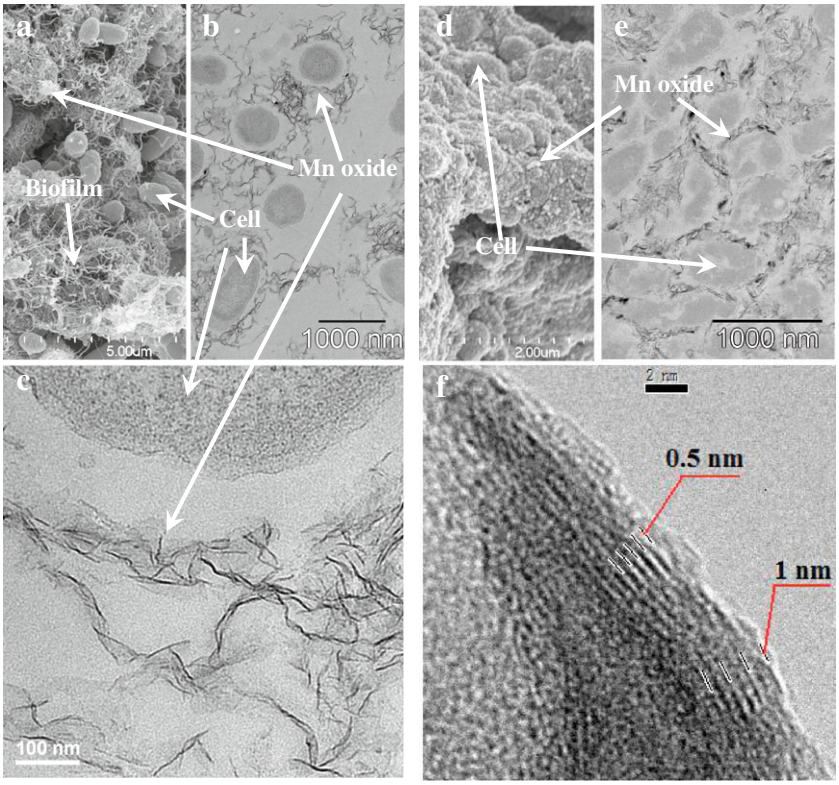

Fig. 6. Electron micrographs of the biogenic Mn oxide produced by *Pseudomonas putida* GB-1 (a–c) and the product (d–f) after Mg^{2+} exchange and reflux treatment for 48 h: (a) FEG-SEM image of the biogenic Mn oxide showing the cells, Mn oxide particles and associated desiccated EPS, (b) TEM image of the biogenic Mn oxide shows the filament or fiber like biogenic Mn oxide surrounding the bacterial cells, (c) HR-TEM of the biogenic Mn oxide shows long and thin sheet morphologies (~50 by 5 nm), (d) FEG-SEM image of the refluxing product shows more closely the association of cells and the Mn oxide particles, (e) TEM image of the refluxing product shows the slightly distorted cells and the peripheral fibrous Mn oxide, (f) HR-TEM image of an individual fiber of the refluxing product shows 1 and 0.5 nm spacings in the *a* direction.

blocks with different tunnel sizes along a^* in the natural and synthetic todorokite samples is quite common (Chukhrov et al., 1979; Turner et al., 1982; Golden et al., 1986; Feng et al., 2004; Bodei et al., 2007). The poorly ordered layer Mn oxide precursor would cause more incoherent tunnel width of the formed todorokites (Bodei et al., 2007). Accordingly, the structural characteristics of biogenic Mn oxide precursor may cause disorder array along a^* in the refluxed products. From the HR-TEM images (Fig. 6), different spacings in the a^* direction were observed. Such morphologic features of variable tunnel sizes along a^* were typical and could be observed in the whole fiber of the refluxed products. The lattice fringes are not very clear due to the low crystallinity and thin layer along c^*. We were unsuccessful in acquiring better images with high resolution and magnification under HR-TEM because the products were slightly sensitive to the electron beam. The lattice fringes with different spacing in the a^* direction indicate that tunnel structures were formed in the products. Thus, the transformation of the biogenic oxide to a todorokite-like phase after refluxing can be illustrated in Fig. 8.

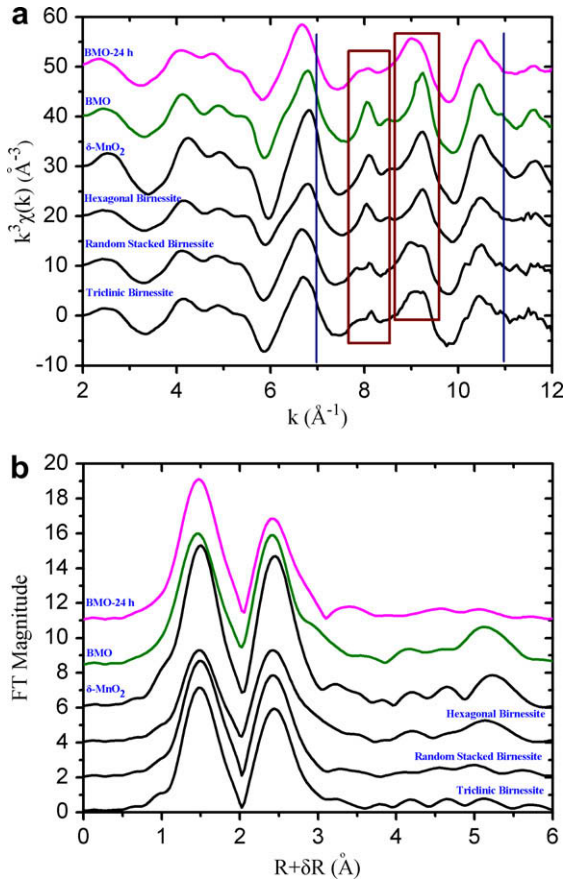

Fig. 7. Mn K-edge k^3-weighted EXAFS (a) and Fourier transformation EXAFS (b) comparison of BMO-24 h and BMO with different phyllomanganites (δ-MnO_2, hexagonal birnessite, random stacked birnessite and triclinic birnessite). Note the change in diagnostic features in the k space region between $k \sim 7$–11 Å^{-1} which is highlighted by the vertical lines.

The poorly crystalline todorokite-like phase formed from biogenic Mn oxides may progressively increase in size and crystallinity to become the final todorokite products under conditions similar to natural todorokite formation described in Buatier et al. (2004). Crystallinity was also observed to increase in the process of natural todorokite formation in hemipelagic sediments (Bodei et al., 2007). In addition, todorokite formed under reflux conditions exhibited increasing XRD peak intensities and crystallinity with reflux time (Feng et al., 2004). However, in this case, the 0.477 and 0.248 nm XRD peaks diagnostic for todorokite decrease in intensity with the reflux time (Fig. 5). This can be ascribed to partial reductive dissolution and the resultant thinner layer of the products as the reflux time increased. The analyses of the reflux solution indicates that the Mn(II) concentration increased from 0 to 20 mg/L and pH increased from 5.1 to above 7.0 when reflux proceeded from 0 to 48 h (Table EA-1). Therefore, the pure Mn oxide system and/or high content of residual biological substances relative to the natural environment and previous reflux system may be the reason that XRD peaks slightly attenuate with the increasing reflux time.

4.3. Implications for the formation of bio-related origin of natural todorokites

Based on data from laboratory and field observations, todorokite does not form directly via a precipitation process (Siegel and Turner, 1983; Golden et al., 1986; Shen et al., 1993; Feng et al., 1995, 1998, 2004; Buatier et al., 2004; Bodei et al., 2007), instead it is likely a product from the transformation of a 10-Å phyllomanganate precursor

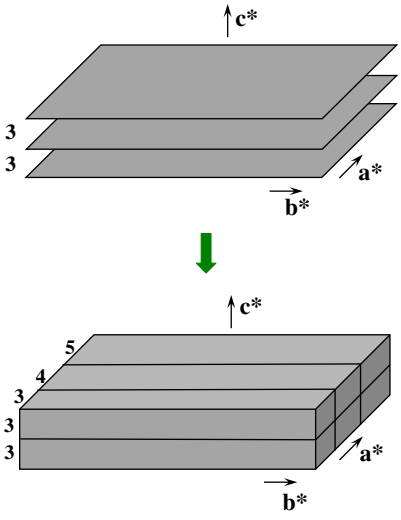

Fig. 8. Diagram of transformation of the biogenic Mn oxide to a todorokite-like phase. The biogenic Mn oxide and the Mg^{2+} exchanged product were thin layer structured phyllomanganates which lack c^* periodicity with interlayer spacing of three MnO_6 octahedra width along c^*. After refluxing, thin tunnel structured todorokite-like phases, which lack c^* periodicity with interlayer spacing of three MnO_6 octahedra width along c^*, and intergrowth with different spacings along a^*, were formed through topotactic transformation.

(Bodei et al., 2007). Recently, a todorokite-like tunnel structural MnO_x formed by the fungus *Acremonium* sp. Strain KR21-2 was reported (Saratovsky et al., 2009). If the above assumption is correct, this fungally mediated MnO_x material may not yield from the primary oxidation of Mn^{2+}, but is a secondary product. The association of biogenic Mn oxide with todorokite, or bio-related origin of todorokite, was observed in many natural environments (Burns and Burns, 1978b; Siegel and Turner, 1983; Buatier et al., 2004; Bodei et al., 2007). Therefore, the simple bio-related formation pathway of natural todorokite can be written as: biogenic Mn oxide → 10-Å phyllomanganate → todorokite. The results of this study provide for the first time the experimental evidence of biogenic Mn oxide transformation to a todorokite-like phase.

Stable 10-Å phyllomanganate is the prerequisite for todorokite formation because its interlayer space matches the $T(3 \times 3)$ tunnel size (Burns et al., 1983; Post and Bish, 1988). Thus interlayer cations with a high enthalpy of hydration, such as Mg^{2+}, Cu^{2+}, Ni^{2+} and Ca^{2+}, are needed to form stable 10-Å phyllomanganate before the todorokite formation. BMO without exchanged Mg^{2+} cannot be converted to as todorokite phase via reflux, but a $T(2 \times 2)$ cryptomelane-like phase forms instead (Fig. EA-2). In addition, as proposed by Bodei et al. (2007), the ideal precursor for defect-free $T(3 \times 3)$ todorokite is a phyllomanganate with high Mn(III); low Mn(III) phyllomanganate results in a highly defective todorokite. The redox conditions, influencing the Mn(III) content in the phyllomanganate, also have effects on the tunnel size of natural todorokite along a^* (Mellin and Lei, 1993; Lei, 1996).

Our recent work also indicates that Mn(III) plays a key role in the transformation of triclinic layered Na-buserite to todorokite via reflux treatment; the transformation from Na-buserite to todorokite decreased gradually with decreasing Mn(III) content (Cui et al., 2008, 2009b). The elongation and weakening of the Mn(III)–O bond in the octahedral layer due to the Jahn-Teller effect will cause the kink-like fold of the layer (Bodei et al., 2007), from which the tunnel walls are constructed. Therefore, in this system, some Mn(III) may be produced by re-oxidation of Mn(II) originating from the partial reductive dissolution of biogenic Mn oxide, which favors todorokite formation. Such Mn(III) production could also account for increased Mn(III) in the refluxed product than its precursor BMO or Todorokite-STD. The symmetry can be changed from triclinic to hexagonal as the Mn(III) content of triclinic birnessite decreases in the layer (Drits et al., 1997; Silvester et al., 1997). On the contrary, it is reasonable to infer that hexagonal phyllomanganates could be converted to triclinic ones with an increase of Mn(III), as the case in this work. The decrease of amplitude in the Mn–Mn multiple scattering peak of 5–6 Å in the *R* space EXAFS spectra (Fig. 3b) and the increase in dihedral angle from out-of-plane bending (Table 1) after reflux also make the inference plausible. Thus, the above todorokite formation pathway can be specified as: hexagonal biogenic Mn oxide → 10-Å triclinic phyllomanganate → todorokite. The more the structure of the precursors departs from 10-Å triclinic phyllomanganate, the more defects the todorokite would exhibit. The failures to obtain todorokite from acid birnessite and 10-Å vernadite, as discussed above, can be explained by lack of enough Mn(III) and hexagonal symmetry in their MnO_6 layer. Furthermore, the kinetics of todorokite transformation from biogenic Mn oxides can be increased by refluxing, which is another reason why todorokite-like phases formed in this study. At the temperature of reflux (100 °C), Mg^{2+}-buserite completely converts to todorokite within 8 h (Feng et al., 2004; Cui et al., 2006). It takes 48 h and 120 h for the similar conversion at 90 °C and 80 °C, respectively. When the temperature is lowered to 40 °C, only part of Mg^{2+}-buserite converts to todorokite even after aging for 35 days. At relatively low temperatures, the rate of todorokite formation decreases sharply (Cui et al., 2006), explaining why todorokite tends to occur prevalently in ocean hydrothermal deposits over diagenetic deposits. Conversely, 10-Å phyllomanganate prevails in diagenetic deposits (Bodei et al., 2007). Consequently, stable 10-Å phyllomanganate, appropriate Mn(III) content and/or triclinic symmetry of the phyllomanganate and relatively high temperature conditions are the three key factors determining todorokite formation. Marine or terrestrial environments which meet with such conditions, such as marine hydrothermal Mn deposits (Usui et al., 1989, 1997; Buatier et al., 2004; Bodei et al., 2007; Takahashi et al., 2007; Dubinin et al., 2008), marine diagenetic Mn concretions (Yoshikawa, 1991; Usui et al., 1997; Takahashi et al., 2007), and soils or sediments enriched with Ca (Taylor et al., 1964; Turner and Buseck, 1981; McKenzie, 1989; Bilinski et al., 2002; Tan et al., 2006; Manceau et al., 2007), are expected to favor todorokite formation.

A two-step dissolution-recrystallization process of natural todorokite formation in ocean nodules was proposed by Burns and Burns (1978b) as follows. First, Mn oxides formed at the surface of detrital matter were partially dissolved by the surrounding organic substances releasing Mn^{2+}; second, the cryptocrystalline Mn oxide of biogenic or abiotic origin, adsorbs the released Mn^{2+} and transforms into todorokite. Bodei et al. (2007) suggested a three-step process of the phyllomanganate to todorokite conversion in ocean sediments, which involves another step of semi-ordered 10-Å phyllomanganate formation before the conversion. The process of todorokite-like phase formation in this study verifies the above assumed processes of todorokite formation in the marine environment. It should be pointed out that the biogenic Mn oxide precursor used in this study was produced by a freshwater bacterium, i.e., *P. putida* strain GB-1, but it will not influence the application of the implications or this work to marine environments due to the similar primary products of microbial Mn(II) oxidation in terms of structure, morphology and crystallinity either by marine bacteria or freshwater bacteria.

5. SUMMARY AND CONCLUSION

The formation pathway of todorokite from layer structured Mn oxides with hexagonal symmetry, biogenic Mn oxides or vernadite (δ-MnO_2), has been speculative due to the lack of direct evidence (Burns and Burns, 1978b;

Mandernack et al., 1995; Post, 1999; Buatier et al., 2004; Bodei et al., 2007). In the present study, it was discovered that a nano-crystalline todorokite-like phase forms from biogenic Mn oxides at atmospheric pressure via a refluxing process. This implies that natural todorokite in marine and terrestrial surface environments may originate from biogenic Mn oxides and is subject to recrystallization from its poorly crystallized form. The symmetry of the phyllomanganates may convert from hexagonal to triclinic, as determined by content of Mn(III) in the MnO_6 layer, before their transformation to todorokite. This fundamental knowledge of biogenic Mn oxide transformation to todorokite is critical to understanding the origin of natural todorokite and the geochemistry of Mn (hydro-) oxide minerals in nature. Furthermore, if different exchangeable cations and solution conditions are present in the above experimental system, other Mn oxides may be expected to form from biogenic Mn oxide through the refluxing process (Fig. EA-2). This process accelerates the rate of transformation reactions of biogenic Mn oxides without apparent damage or dissolution. This will facilitate our ability to investigate the relationship and underlying mechanisms for biogenic Mn oxide transformation, a process commonly occurring in ocean Mn deposits and soil ferromanganese aggregates, and the biosynthesis of various porous OMS nano-crystallites. It is hoped that our results will help to stimulate such investigations.

ACKNOWLEDGEMENTS

We thank S.M. Webb and K. Pandya for their technical support with the SR-XRD and XAFS analyses. We are grateful to K. Czymmek, S. Modla and D. Powell for their help with the FEG-SEM and TEM analyses. We thank Dr. Jeffrey E. Post (Smithsonian Institution, Washington, DC) for his insightful review of the manuscript prior to submission. We gratefully acknowledge the two anonymous reviewers for their critical and very helpful comments on the manuscript. X.F. Feng thanks the Natural Science Foundation of China (Nos. 40830527 and 40971142), Program for New Century Excellent Talents in University and the Foundation for the Author of National Excellent Doctoral Dissertation of PR China (No. 200767) for financial support.

APPENDIX A. SUPPLEMENTARY DATA

Supplementary data associated with this article can be found, in the online version, at doi:10.1016/j.gca.2010.03.005.

REFERENCES

Bargar J. R., Tebo B. M., Bergmann U., Webb S. M., Glatzel P., Chiu V. Q. and Villalobos M. (2005) Biotic and abiotic products of Mn(II) oxidation by spores of the marine *Bacillus* sp. strain SG-1. *Am. Mineral.* **90**, 143–154.

Bargar J. R., Fuller C. C., Marcus M. A., Brearley A. J., De la Rosa M. P., Webb S. M. and Caldwell W. A. (2009) Structural characterization of terrestrial microbial Mn oxides from Pinal Creek, AZ. *Geochim. Cosmochim. Acta* **73**, 889–910.

Bilinski H., Giovanoli R., Usui A. and Hanzel D. (2002) Characterization of Mn oxides in cemented streambed crusts from Pinal Creek, Arizona, USA, and in hot-spring deposits from Yuno-Taki falls, Hokkaido, Japan. *Am. Mineral.* **87**, 580–591.

Bodei S., Manceau A., Geoffroy N., Baronnet A. and Buatier M. (2007) Formation of todorokite from vernadite in Ni-rich hemipelagic sediments. *Geochim. Cosmochim. Acta* **71**, 5698–5716.

Boogerd F. C. and de Vrind J. P. M. (1987) Manganese oxidation by *Leptothrix discophora*. *J. Bacteriol.* **169**, 489–494.

Buatier M. D., Guillaume D., Wheat C. G., Herve L. and Adatte T. (2004) Mineralogical characterization and genesis of hydrothermal Mn oxides from the flank of the Juan the Fuca Ridge. *Am. Mineral.* **89**, 1807–1815.

Burle E. and Kirby-Smith W. W. (1979) Application of formaldoxime colorimetric method for the determination of manganese in the pore water of anoxic estuarine sediments. *Estuar. Coast.* **2**, 198–201.

Burns V. M. and Burns R. G. (1978a) Authigenic todorokite and phillipsite inside deep-sea manganese nodules. *Am. Mineral.* **63**, 827–831.

Burns V. M. and Burns R. G. (1978b) Post-depositional metal enrichment processes inside manganese nodules from the north equatorial Pacific. *Earth Planet. Sci. Lett.* **39**, 341–348.

Burns R. G., Burns V. M. and Stockman H. (1983) A review of the todorokite–buserite problem: implications to the mineralogy of marine manganese nodules. *Am. Mineral.* **68**, 972–980.

Burns R. G., Burns V. M. and Stockman H. (1985) The todorokite–buserite problem: further consideration. *Am. Mineral.* **68**, 972–980.

Buser W. and Grütter A. (1956) Ueber die Natur der Mangannollen. *Schweiz. Mineral. Petrogr. Mitt.* **36**, 49–62.

Ching S., Krukowska K. S. and Suib S. L. (1999) A new synthetic route to todorokite-type manganese oxides. *Inorg. Chim. Acta* **294**, 123–132.

Chukhrov F. V., Gorshkov A., Sivtsov A. V. and Berezovskaya V. V. (1979) New data on natural todorokites. *Nature* **278**, 631–632.

Cui H. J., Feng X. H., He J. Z., Tan W. F. and Liu F. (2006) Effects of reaction conditions on the formation of todorokite at atmospheric pressure. *Clays Clay Miner.* **54**, 605–615.

Cui H. J., Liu X. W., Tan W. F., Feng X. H., Liu F. and Ruan H. D. (2008) Influence of Mn(III) availability on the phase transformation from layered buserite to tunnel-structured todorokite. *Clays Clay Miner.* **56**, 397–403.

Cui H. J., Feng X. H., Tan W. F., He J. Z., Hu R. G. and Liu F. (2009a) Synthesis of todorokite-type manganese oxide from Cu-buserite by controlling the pH at atmospheric pressure. *Micropor. Mesopor. Mater.* **117**, 41–47.

Cui H. J., Qiu G. H., Feng X. H., Tan W. F. and Liu F. (2009b) Birnessites with different average manganese oxidation states were synthesized, characterized, and transformed to todorokite at atmospheric pressure. *Clays Clay Miner.* **57**(6), 715–724.

Dixon J. B. and Skinner H. C. W. (1992) Manganese minerals in surface environments. In *Biomineralization Processes of Iron and Manganese. Modern and Ancient Environments* (eds. H. C. W. Skinner and R. W. Fitzpatrick). CATENA Verlag, Cremlingen-Destedt, Germany.

Drits V. A., Silvester E., Gorshkov A. I. and Manceau A. (1997) The structure of synthetic monoclinic Na-rich birnessite and hexagonal birnessite. Part 1. Results from X-ray diffraction and selected area electron diffraction. *Am. Mineral.* **82**, 946–961.

Dubinin A., Uspenskaya T., Gavrilenko G. and Rashidov V. (2008) Geochemistry and genesis of Fe–Mn mineralization in island arcs in the west Pacific Ocean. *Geochem. Int.* **46**, 1206–1227.

Feng Q., Kanoh H., Miyai Y. and Ooi K. (1995) Metal ion extraction/insertion reactions with todorokite-type manganese oxide in the aqueous phase. *Chem. Mater.* **7**, 1722–1727.

Feng Q., Yanagisawa K. and Yamasaki N. (1998) Hydrothermal soft chemical process for synthesis of manganese oxides with tunnel structures. *J. Porous Mater.* **5**, 153–161.

Feng Q., Kanoh H. and Ooi K. (1999) Manganese oxide porous crystals. *J. Mater. Chem.* **9**, 319–333.

Feng X. H., Tan W. F., Liu F., Wang J. B. and Ruan H. D. (2004) Synthesis of todorokite at atmospheric pressure. *Chem. Mater.* **16**, 4330–4336.

Feng X. H., Zhai L. M., Tan W. F., Liu F. and He J. Z. (2007) Adsorption and redox reactions of heavy metals on synthesized Mn oxide minerals. *Environ. Pollut.* **147**, 366–373.

Gadde R. R. and Laitinen H. A. (1974) Studies of heavy metal adsorption by hydrous iron and manganese oxides. *Anal. Chem.* **46**(13), 2022–2026.

Glasby G. P. (2006) Manganese: predominant role of nodules and crusts. In *Marine Geochemistry* (eds. H. D. Schulz and M. Zabel). Springer, pp. 371–427.

Giovanoli R. (1985) A review of the todorokite–buserite problem: implications to the mineralogy of marine manganese nodules: discussion. *Am. Mineral.* **70**, 202–204.

Goldberg E. D. (1954) Marine geochemistry I. Chemical scavengers of the sea. *J. Geol.* **62**, 249–265.

Golden D. C., Chen C. C. and Dixon J. B. (1986) Synthesis of todorokite. *Science* **231**, 717–719.

Golden D. C., Chen C. C. and Dixon J. B. (1987) Transformation of birnessite to buserite, todorokite, and manganite under mild hydrothermal treatment. *Clays Clay Miner.* **35**, 271–280.

Hammersley A. P., Svensson S. O., Han M., Fitch A. N. and Hausermann D. (1996) Two-dimensional detector software: from real detector to idealised image or two-theta scan. *High Press. Res.* **14**, 235–248.

Kim H. S., Pasten P. A., Gaillard J. F. and Stair P. C. (2003) Nanocrystalline todorokite-like manganese oxide produced by bacterial catalysis. *J. Am. Chem. Soc.* **125**, 14284.

Lanson B., Drits V. A., Feng Q. and Manceau A. (2002) Crystal structure determination of synthetic Na-rich birnessite: evidence for a triclinic one-layer cell. *Am. Mineral.* **87**, 1662–1671.

Lei G. B. (1996) Crystal structures and metal uptake capacity of 10 angstrom-manganates: an overview. *Mar. Geol.* **133**, 103–112.

Liu Z. H., Kang L., Ooi K., Yoji M. and Feng Q. (2005) Studies on the formation of todorokite-type manganese oxide with different crystalline birnessites by Mg^{2+}-templating reaction. *J. Colloid Interface Sci.* **285**, 239–246.

Luo J., Zhang Q., Huang A., Giraldo O. and Suib S. L. (1999) Double-aging method for preparation of stabilized Na-buserite and transformations to todorokites incorporated with various metals. *Inorg. Chem.* **38**, 6106–6113.

Manceau A., Tommaseo C., Rihs S., Geoffroy N., Chateigner D., Schlegel M., Tisserand D., Marcus M. A., Tamura N. and Chen Z. S. (2005) Natural speciation of Mn, Ni, and Zn at the micrometer scale in clayey paddy soil using X-ray fluorescence, absorption, and diffraction. *Geochim. Cosmochim. Acta* **69**, 4007–4034.

Manceau A., Kersten M., Marcus M. A., Geoffroy N. and Granina L. (2007) Ba and Ni speciation in a nodule of binary Mn oxide phase composition from Lake Baikal. *Geochim. Cosmochim. Acta* **71**, 1967–1981.

Mandernack K. W., Post J. and Tebo B. M. (1995) Manganese mineral formation by bacterial spores of the marine *Bacillus*, strain SG-1: evidence for the direct oxidation of Mn(II) to Mn(IV). *Geochim. Cosmochim. Acta* **59**, 4393–4408.

McKenzie R. M. (1989) Manganese oxides and hydroxides. In *Minerals in Soil Environments*, second ed. (eds. J. B. Dixon and S. B. Weed). SSSA Book Series No. 1. SSSA Inc. pp. 439–465.

McKenzie R. M. (1971) The synthesis of birnessite, cryptomelane, and some other oxides and hydroxides of manganese. *Miner. Mag.* **38**, 493–503.

McKeown D. A. and Post J. E. (2001) Characterization of manganese oxide mineralogy in rock varnish and dendrites using X-ray absorption spectroscopy. *Am. Mineral.* **86**, 701–713.

Mellin T. A. and Lei G. (1993) Stabilization of 10 Å-manganates by interlayer cations and hydrothermal treatment: implications for the mineralogy of marine manganese concretions. *Mar. Geol.* **115**, 67–83.

Miyata N., Tani Y., Maruo K., Tsuno H., Sakata M. and Iwahori K. (2006) Manganese(IV) oxide production by *Acremonium* sp. strain KR21-2 and extracellular Mn(II) oxidase activity. *Appl. Environ. Microbiol.* **72**, 6467–6473.

Nealson K. H., Tebo B. M. and Rosson R. A. (1988) Occurrence and mechanisms of microbial oxidation of manganese. *Adv. Appl. Microbiol.* **33**, 279–318.

Parikh S. J. and Chorover J. (2005) FTIR spectroscopic study of biogenic Mn-oxide formation by *Pseudomonas putida* GB-1. *Geomicrobiol. J.* **22**, 207–218.

Post J. E. and Bish D. L. (1988) Rietveld refinement of the todorokite structure. *Am. Mineral.* **73**, 861–869.

Post J. E. (1999) Manganese oxide minerals: crystal structures and economic and environmental significance. *Proc. Natl. Acad. Sci. USA* **96**, 3447–3454.

Saratovsky I., Wightman P. G., Pasten P. A., Gaillard J. F. and Poeppelmeier K. R. (2006) Manganese oxides: parallels between abiotic and biotic structures. *J. Am. Chem. Soc.* **128**, 11188–11198.

Saratovsky I., Gurr S. J. and Hayward M. A. (2009) The structure of manganese oxide formed by the fungus *Acremonium* sp. strain KR21-2. *Geochim. Cosmochim. Acta* **73**, 3291–3300.

Silvester E., Manceau A. and Drits V. A. (1997) The structure of synthetic monoclinic Na-rich birnessite and hexagonal birnessite. Part 2. Results from chemical studies and EXAFS spectroscopy. *Am. Mineral.* **82**, 962–978.

Shen Y. F., Zerger R. P., DeGuzman R. N., Suib S. L., McCurdy L., Potter D. I. and O'Young C. L. (1993) Manganese oxide octahedral molecular sieves: preparation, characterization and application. *Science* **260**, 511–515.

Siegel M. D. and Turner S. (1983) Crystalline todorokite associated with biogenic debris in manganese nodules. *Science* **219**, 172–174.

Suib S. L. (2008) Structure, porosity, and redox in porous manganese oxide octahedral layer and molecular sieve materials. *J. Mater. Chem.* **18**, 1623–1631.

Tan W. F., Liu F., Li Y. H., Hu H. Q. and Huang Q. Y. (2006) Elemental composition and geochemical characteristics of iron–manganese nodules in main soils of China. *Pedosphere* **16**(1), 72–81.

Taylor R. M., McKenzie R. M. and Norrish K. (1964) The mineralogy and chemistry of manganese in some Australian soils. *Aust. J. Soil Res.* **2**, 235–248.

Takahashi Y., Manceau A., Geoffroy N., Marcus M. A. and Usui A. (2007) Chemical and structural control of the partitioning of Co, Ce, and Pb in marine ferromanganese oxides. *Geochim. Cosmochim. Acta* **71**, 984–1008.

Takematsu N., Sato Y. and Okabe S. (1984) The formation of todorokite and birnessite in sea water pumped from under ground. *Geochim. Cosmochim. Acta* **48**, 1099–1106.

Takematsu N., Kusakabe H., Sato Y. and Okabe S. (1988) Todorokite formation in seawater by microbial mediation. *J. Oceanogr. Soc. Jpn.* **44**, 235–243.

Tebo B. M., Bargar J. R., Clement B. G., Dick G. J., Murray K. J., Parker D., Verity R. and Webb S. M. (2004) Biogenic

manganese oxides: properties and mechanisms of formation. *Annu. Rev. Earth Planet. Sci.* **32**, 287–328.

Toner B., Fakra S., Villalobos M., Warwick T. and Sposito G. (2005) Spatially resolved characterization of biogenic manganese oxide production within a bacterial biofilm. *Appl. Environ. Microbiol.* **71**, 1300–1310.

Turner S. and Buseck P. R. (1981) Todorokites: a new family of naturally occurring manganese oxides. *Science* **212**, 1024–1027.

Turner S., Siegel M. D. and Buseck P. R. (1982) Structural features of todorokite intergrowths in manganese nodules. *Nature* **296**, 841–842.

Usui A., Mellin T. A., Nohara M. and Yuasa M. (1989) Structural stability of marine 10 Å manganates from the Ogasawara (Bonin) arc: implication for low-temperature hydrothermal activity. *Mar. Geol.* **86**, 41–56.

Usui A., Bau M. and Yamazaki T. (1997) Manganese microchimneys buried in the Central Pacific pelagic sediments: evidence of intraplate water circulation? *Mar. Geol.* **141**, 269–285.

Vileno E., Ma Y., Zhou H. and Suib S. L. (1998) Facile synthesis of synthetic todorokite (OMS-1), co-precipitation reactions in the presence of a microwave field. *Micropor. Mesopor. Mater.* **20**, 3–15.

Villalobos M., Lanson B., Manceau A., Toner B. and Sposito G. (2006) Structural model for the biogenic Mn oxide produced by *Pseudomonas putida*. *Am. Mineral.* **91**, 489–502.

Villalobos M., Toner B., Bargar J. and Sposito G. (2003) Characterization of the manganese oxide produced by *Pseudomonas putida* strain MnB1. *Geochim. Cosmochim. Acta* **67**, 2649–2662.

Webb S. M. (2005) SIXPACK: a graphical user interface for XAS analysis using IFEFFIT. *Phys. Scr.* **T115**, 1011–1014.

Webb S. M., Fuller C. C., Tebo B. M. and Bargar J. R. (2006) Determination of uranyl incorporation into biogenic manganese oxides using X-ray absorption spectroscopy and scattering. *Environ. Sci. Technol.* **40**, 771–777.

Webb S. M., Tebo B. M. and Bargar J. R. (2005a) Structural characterization of biogenic manganese oxides produced in seawater by the marine *Bacillus* sp. strain SG-1. *Am. Mineral.* **90**, 1342–1357.

Webb S. M., Tebo B. M. and Bargar J. R. (2005b) Structure influence of sodium and calcium ions on the biogenic manganese oxides produced by the marine *Bacillus* sp. strain SG-1. *Geomicrobiol. J.* **22**, 181–193.

Yang D. S. and Wang M. K. (2002) Syntheses and characterization of birnessite by oxidizing pyrochroite in alkaline conditions. *Clays Clay Miner.* **50**, 63–69.

Yoshikawa K. (1991) The relationship between manganese minerals and metallic elements in deep-sea manganese nodules. *Mar. Geol.* **101**, 267–286.

Associate editor: Jon Chorover